Lab on a Chip

A Wearable Electrofluidic Actuation System

Journal:	*Lab on a Chip*
Manuscript ID	LC-COM-05-2019-000454.R1
Article Type:	Communication
Date Submitted by the Author:	08-Jul-2019

Complete List of Authors:	Lin, Haisong; University of California Los Angeles, Electrical and Computer Engineering Hojaiji, Hannaneh; University of California Los Angeles Henry Samueli School of Engineering and Applied Science, Electrical and Computer Engineering Lin, Shuyu; University of California Los Angeles, Electrical and Computer Engineering Yeung, Christopher; University of California Los Angeles, Materials Science and Engineering Zhao, Yichao; University of California Los Angeles Wang, Bo; University of California, Los Angeles, Chemical and Biomolecular Engineering Malige, Meghana; University of California Los Angeles, Electrical and Computer Engineering Wang, Yibo; University of California Los Angeles, Electrical and Computer Engineering King, Kimber; University of California Los Angeles, Electrical and Computer Engineering Yu, Wenzhuo; University of California Los Angeles, Electrical and Computer Engineering Tan, Jiawei; University of California Los Angeles, Materials Science and Engineering Wang, Zhaoqing; University of California Los Angeles, Electrical and Computer Engineering Cheng, Xuanbing; University of California Los Angeles, Materials Science and Engineering Emaminejad, Sam; University of California Los Angeles, Electrical and Computer Engineering

A Wearable Electrofluidic Actuation System

Haisong Lin[1†], Hannaneh Hojaiji[1†], Shuyu Lin[1†], Christopher Yeung[1,2], Yichao Zhao[1,2], Bo Wang[1], Meghana Malige[1], Yibo Wang[1], Kimber King[1], Wenzhuo Yu[1], Jiawei Tan[1,2], Zhaoqing Wang[1], Xuanbing Cheng[1,2] and Sam Emaminejad[1*]

[1] Department of Electrical and Computer Engineering, University of California, Los Angeles, CA, USA

[2] Department of Materials Science and Engineering, University of California, Los Angeles, CA, USA

[†] These authors contributed equally to this work.

[*] Correspondence and requests for materials should be addressed to S.E. (emaminejad@ucla.edu)

Abstract

We report a wearable electrofluidic actuation system, which exploits the alternating current electrothermal (ACET) effects to engineer biofluid flow profiles on body. The wearable ACET flow is induced with the aid of corrosion-resistant electrode configurations (fabricated on a flexible substrate) and a custom-developed, wirelessly programmable high frequency (MHz) excitation circuitry. Various tunable flow profiles are demonstrated with the aid of the devised flexible ACET electrode configurations, where the induced profiles were in agreement with the ACET theory and simulation. The demonstrated capabilities rendered by the presented system create new degrees of freedom for implementing advanced bioanalytical operations for future lab-on-the-body platforms.

Recent advances in electrochemical sensor development, flexible microfluidic device fabrication, and design and implementation of low-power electronics have paved a path toward (semi)continuous monitoring of the body's dynamic chemistry by analyzing molecular-level biomarkers in biofluids such as sweat [1-7]. Previously reported wearable biomarker sensors successfully demonstrated electrochemical and colorimetric sensing interfaces, incorporated within microfluidic channels, for on-body detection of analytes (in micro- to millimolar ranges) [8-14]. However, their passive control of fluid inherently limits their analytical operations. As previously shown in the context of lab-on-a-chip devices, active fluidic control (*e.g.*, mixing) can create new degrees of freedom for the implementation of auxiliary sample manipulation operations to realize a broad range of assays in order to target a diverse set of biomarkers [15-18]. Such assays can in principle be adapted for wearable biomarker analysis by exploiting the readily small footprint of their transduction interfaces. However, the challenge remains in creating active biofluid actuation capabilities that can be performed in a wearable format.

To this end, electrofluidic-based actuation techniques are suitable, given their miniaturized interface and electronic programmability [19-27]. In that regard, two main problems need to be addressed: 1) devising a durable, corrosion-resistant and flexible electrofluidic interface, which can reliably perform actuation in biofluidic conditions and 2) developing a wearable and battery-powered control electronic circuitry that can deliver the required excitation voltage levels at relatively high frequencies (~ in MHz range). The latter, essentially, necessitates miniaturization of bulky and power outlet-connected excitation instruments, which are used by conventional lab-on-a-chip-based platforms to perform electrofluidic actuation [28].

Here, we particularly exploit the alternating current electrothermal (ACET) flow phenomenon to render on-demand, programmable, and precise microfluidic actuation. ACET-based actuation techniques have been proven to be effective in manipulating fluids with high conductivity [20-23] (*e.g.*, biofluids). Alternative electro-fluidic flow actuation techniques such as AC electroosmosis (ACEO) [27] and electrowetting-on-dielectric (EWOD) [29,30] may not be suitable for wearable applications due to their stringent requirements for low-conductivity fluids and/or high operation voltages.

To realize wearable ACET actuation, we fabricated and embedded corrosion-resistant electrode configurations (patterned on a flexible substrate) within a microfluidic device and custom-developed a wirelessly programmable high frequency (MHz) excitation circuitry. The performance of the ACET electrode configurations were characterized in relation to the induced flow profiles, and a representative on-body actuation operation was validated through human subject testing with our wearable actuation system.

Results and discussion

ACET flow arises in the presence of a temperature gradient induced by a non-uniform electric field. By applying an AC voltage across a pair of coplanar electrodes, a non-uniform electric field $\mathbf{E}$ (magnitude represented as E) is established, which results in a temperature gradient profile (∇T) inside the microfluidic channel (conceptualized in Fig. S1a,b). This temperature gradient correspondingly produces gradients in permittivity ($\nabla\varepsilon = (\partial\varepsilon/\partial T)\nabla T$) and conductivity ($\nabla\sigma = (\partial\sigma/\partial T)\nabla T$)). The interaction of the electric field with these gradient profiles results in a body force ($\mathbf{f}_\mathrm{E}$) acting on the fluid, governed by the equation [20]:

$$\mathbf{f}_{\mathrm{E}} = [\frac{\sigma_0 \nabla \varepsilon - \varepsilon_0 \nabla \sigma}{\sigma_0 + i\omega\varepsilon_0} \cdot \mathbf{E}_0]\mathbf{E}_0 - \frac{1}{2}E_0^2 \nabla \varepsilon \quad (1)$$

, where subscript 0 describes the physical variable at a spatially constant temperature (*e.g.*, $\mathbf{E}_0$ is the electric field at a spatially constant temperature, $T = T_0$). The generated body force induces fluid motion (Fig. S1c) with a velocity that is proportional to $E_0^2 \nabla T$ (as described supplementary materials). In this case, since ∇T is induced by the electric field (where $\nabla T \propto E^2$), the velocity becomes proportional to E^4, or the 4th power of the applied voltage. To exploit the ACET flow phenomenon for inducing a net flow, asymmetric configurations can be utilized. As conceptualized in Fig. 1 a,b and Fig. S1, by changing the symmetric ACET electrode design to an asymmetric configuration, imbalanced electric and temperature field profiles can be generated, which in turn leads to breaking the symmetry of competitive flow vortices and inducing a net flow (Fig. 1a,b).

To realize ACET flow within a wearable electrofluidic actuation platform, a flexible tape-based epidermal microfluidic device is developed (Fig. 1c, d). The ACET electrodes are patterned onto a flexible polyethylene terephthalate (PET) substrate and incorporated into a tape-based flexible microfluidic device (Fig. 1e). The electrode layers are fabricated by deposition and patterning of 20 nm Cr (for metal adhesion)-100 nm Au-20 nm Ti. The incorporation of the Ti layer was to realize a biofluid-facing electrolysis-resistant layer to ensure long-term and stable operation. The microfluidic system is constructed by stacking layers of laser-patterned double-sided tape (forming the microfluidic channel) on the ACET electrode-patterned PET substrate, followed by a PET ceiling to seal the device. To further avoid electrolysis and to bypass the double layer capacitance formed at the interface of the electrode-biofluid [22], the electrodes are excited with an AC voltage source at a sufficiently high frequency (8 MHz).

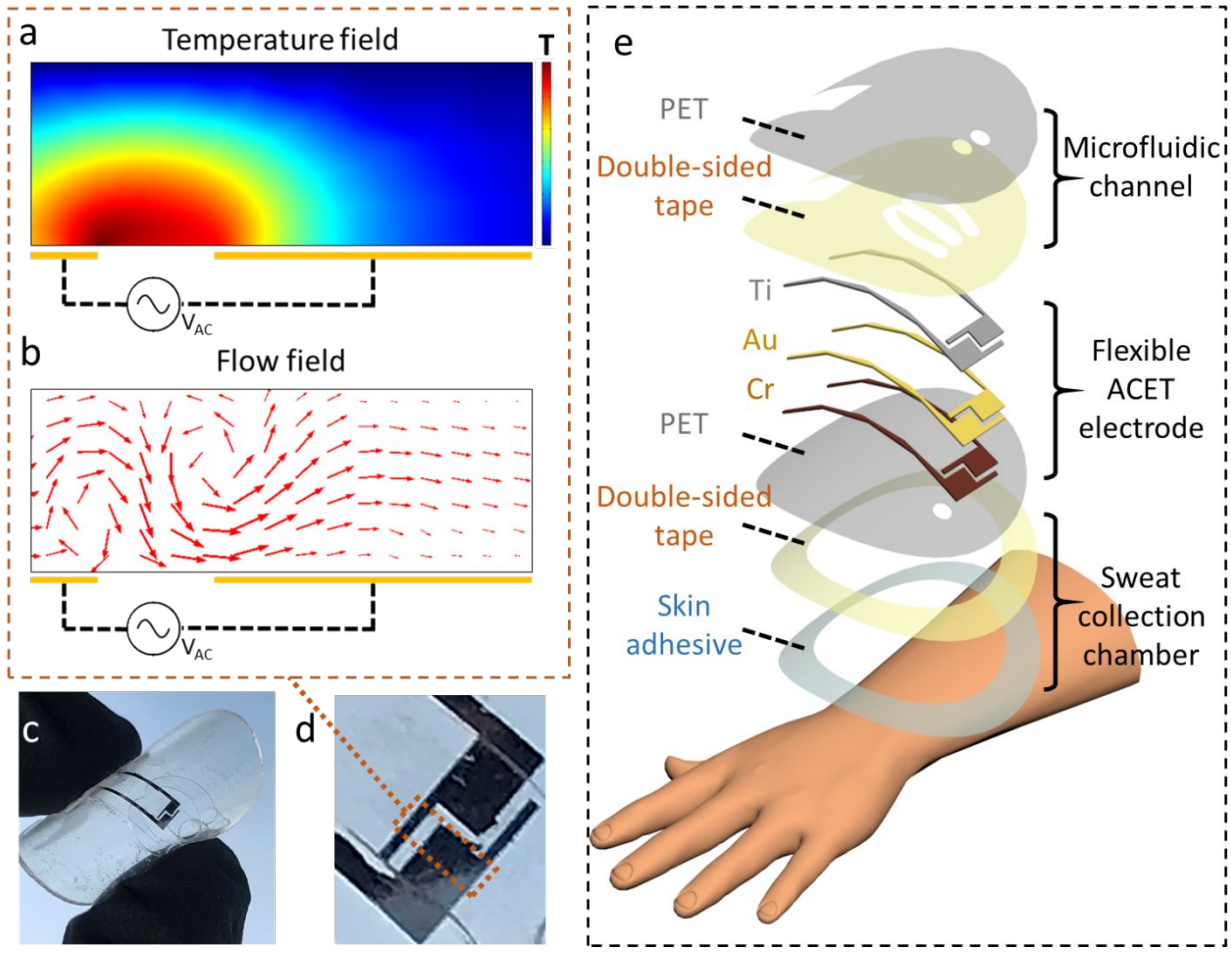

Fig. 1. Wearable ACET actuation: a,b) Conceptual illustrations of the ACET-induced temperature (a) and flow field (b) profiles, generated by an asymmetric coplanar pair of electrodes. c,d) Epidermal microfluidic device with an embedded ACET electrode pair. e) Exploded view of the epidermal microfluidic device structure.

To verify the ACET actuation phenomenon, two configurations of asymmetric electrodes are devised, which induce directional fluid flow, and allow for characterizing their velocity profiles in response to the excitation voltage levels. The first configuration is based on a previously reported asymmetric parallel electrode pair consisting of a narrow electrode (width: 40 μm) and a wide electrode (width: 90 μm), separated by 10 μm (Fig. 2a, c) [20]. In that regard, it is postulated that the wide electrode has a larger effective area of fluid induction compared to the narrow electrode, thus driving the direction of the flow [20]. The second design (Fig. 2b, d) is based on our devised

three identical parallel electrodes (width and spacing: 250 μm) positioned 250 μm away from a single orthogonally oriented electrode (width: 250 μm). It can be noted that in this configuration, the region with highest ∇T appears between the tips of the parallel electrodes and the single orthogonally oriented electrode. As a result, the induced flow in the middle region (between the orthogonal electrodes) dominates the surrounding region and creates a directional flow. The electrothermal simulation, shown in Fig. 2a-d, verifies that the devised asymmetric electrode configurations result in directional flow profiles (the simulation details are explained in the supplementary materials.). To validate and characterize the flow induced by these configurations, 6 μm-diameter beads were introduced into the ACET electrode-patterned channel, and by applying different voltage levels, a range of flow velocities were achieved and characterized (Supplementary video 1). Here, the corresponding induced velocities were estimated by sequentially imaging the advective motion of the beads. Figure 2g, h illustrate that the measured velocity values for both configurations are proportional to the 4^{th} power of the applied voltage, which is in agreement with the expected electrothermal flow velocity-voltage relationship (as described above). Fundamentally, the maximum voltage for ACET-based operations is limited by electrolysis and degassing/boiling, as previously thoroughly analyzed in the context of conventional microfluidic devices [31].

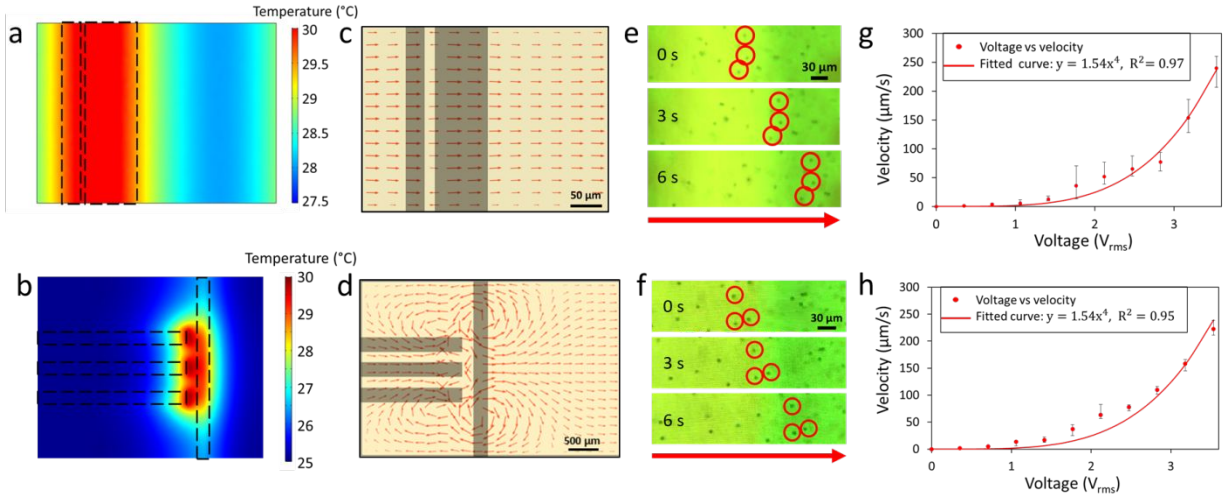

Fig. 2. Directional ACET flow simulation and characterization: a, b) Simulated thermal profiles of parallel (a) and orthogonal (b) electrode configurations (top-view). c, d) The respective simulated ACET-induced velocity profiles illustrating net fluid direction (top-view). e, f) Sequential images of microbeads moving downstream of the channel due to the ACET directional flow (at t = 0 s, 3 s, 6 s). g, h) Characterization of the induced velocities for a range of applied voltages, indicating velocity is proportional to the 4th power of applied voltage.

Through the elaborate design of the ACET electrode configurations, the induced flow profile can be engineered to deliver the intended operations. For example, to achieve mixing of neighboring laminar flow streams, a rotationally symmetric electrode pair configuration can be used [26], which induces local in-plane micro-vortex flow profile. As shown in the context of conventional lab-on-a-chip devices, electrofluidic mixing can be used to overcome laminar flow limitations when introducing external reagents to implement complex bioassay, as well as to enhance analyte transport onto the sensing interface, both of which can be potentially adopted for on-body applications [24-26]. As shown in Fig. 3a, b, the electrothermal simulation validates the induction of stirring-like fluid flow profile. In order to evaluate the mixing performance of this configuration, the mixing electrode pair is used to induce mixing of two neighboring injected laminar fluid flows (one 1X phosphate buffered saline, PBS, another 0.2X PBS dyed with Rhodamine B for

visualization, injected by two syringe pumps in parallel) downstream of a reverse-bifurcated channel (Fig. 3c). In this way, the effect of locally generated flow vortices (as induced by these electrodes) can be characterized against pressure-driven flow profiles. As observed experimentally (Fig. S2), the induced vortices are initially most significant at the end-junctions in-between the narrow and wide electrodes, where the flow field is strongest (as visualized by the simulation results in Fig. 3b). This phenomenon can also be observed for different scaled configurations, as illustrated in Fig. S3, where we simulated the effect of device/channel scaling on ACET actuation performance.

Similar to previous mixing characterization efforts [25], a mixing index is defined (supplementary materials), which effectively captures the reciprocal of the standard deviation of the local dye density in the imaged region (the higher the index value, the lower the standard deviation, and the more uniform the local dye density in the imaged region). This index is linearly mapped over the range of 0 to 1, where 0 corresponds to the initial state with flow rate of 10 uL/min (negligible passive mixing), and 1 corresponds to the fully-mixed steady state where the whole image is homogeneous (*e.g.*, at minute 2 of mixing for flow rate of 0.5uL/min) (Fig. 3d). Due to its electro-fluidic nature, this mixing capability can be precisely tuned by programming the applied voltage at the electrodes (Supplementary video 2).

The temporal mixing progression was characterized under different applied voltage levels (at constant flow rate of 1.5 μL/min, corresponding to the typical sweat rate induced when iontophoretically stimulating 1 cm^2 of skin area). As shown in Fig. 3e, an increasing mixing index with the applied voltage can be observed, where the steady state is reached within about three

minutes upon activation of ACET. The ACET-induced stirring capability was further characterized under a range of flow rates (at constant applied voltage of 3.5 V_{rms}) and compared with passive mixing (without ACET actuation). As shown in Fig. 3f, the mixing index in both cases of passive and active mixing increases with decreasing flow rate (as expected, because of the smaller Péclet number), while in all scenarios, the induction of ACET flow results in the enhancement of the mixing efficiency.

The stability and robustness of the ACET actuation system for envisioned wearable applications is illustrated in Fig. S4a, where it can be observed that the intended mixing operation is achieved over an extended amount of time (> 8 hr) and at high ambient temperatures (*e.g.*, 40 °C). Additionally, the mixing performance is evaluated by placing the device at various angles (0-90^o, to simulate the device orientation conditions on body) and characterizing the mixing index for both cases of with and without ACET actuation. The results show that for all orientation angles, mixing takes place at significantly faster rate for the ACET-induced cases as compared to that of the passive mixing cases (Fig. S4b). For practical applications, the influence of variation in biofluid ionic strength on the intended ACET actuation performance must also be considered. Generally, higher biofluid ionic strength (*i.e.*, higher biofluid salt concentration) results in higher conductivity of the solution, and thus, higher temperature, which leads to establishing greater temperature gradient and stronger electrothermal body forces inside the channel (Equation 8 in Supplementary Information). Therefore, in the context of ACET mixing, a higher mixing efficiency should be expected for higher solution conductivity. To demonstrate this point, we specifically repeated the ACET mixing efficiency characterization experiment for solutions with different salt concentration levels, and simulated the corresponding ACET-induced velocity. The results

indicate that with higher fluid conductivity, both the mixing efficiency and induced velocity enhance (Fig. S5). While the results demonstrate that the intended mixing profile is achieved, if precise control on the biofluid actuation is desired, auxiliary conductivity sensing interface may be incorporated to adjust the excitation level accordingly.

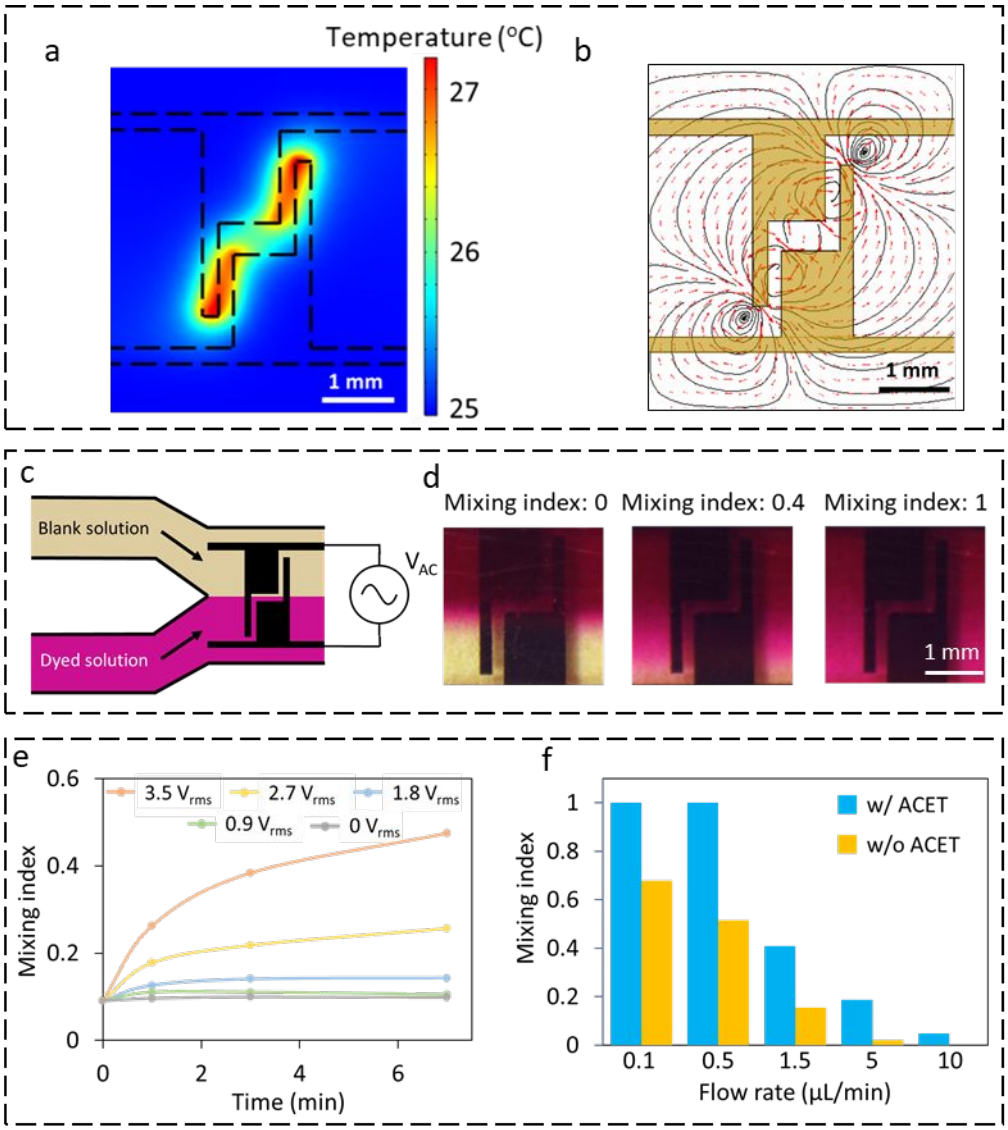

Figure 3. ACET mixing simulation and characterization. a) Simulated thermal profile of rotationally symmetric electrodes for ACET mixing (applied voltage: 3.5 V_{rms}). b) The respective simulated ACET-induced velocity profile, illustrating a vortex-like fluid motion (velocity field and vector are correspondingly shown with streamlines and arrows). c) Experimental setup for the ACET mixing of two fluids (blank and dyed solutions). d) Optical images corresponding to mixing indices of 0, 0.4 and 1. e) Mixing index *vs.* time for a range of applied voltages (externally driven

flow rate: 1.5 μL/min). f) Comparison of mixing index *vs.* flow rate with and without ACET actuation (captured at t = 2 min, applied voltage: 3.5 V_{rms}).

To address the bottleneck of ACET actuation with a wearable high frequency excitation system, we leverage a push-pull transistor-based configuration, which generates a symmetric sinusoidal signal within the required voltage (0-3.5 V_{rms}) and frequency (~1-8 MHz) ranges (Fig. 4a-e). This transistor configuration is driven with the aid of a microcontroller unit (MCU, ATmega328 – TQFP, Atmel), which additionally facilitates system level functionalities, including user-initiated command processing and data communication. As shown in Fig. 4a and Fig. S6, the gate signals of the push-pull transistors are controlled by using the MCU's 8 MHz Pulse-Width-Modulation (PWM) output as an input control signal to output an amplified symmetric sinusoidal signal (Fig. 4b). The PWM temporal characteristics are defined by programming the MCU's timer prescalers to generate a 50% duty cycle. The step-up and negative charge pump converters provide the voltages needed for the positive and negative rails of the transistors. To achieve a symmetric excitation signal, an AC coupling capacitor is included at the output (Fig. S6). A digital switch is incorporated in the system design to facilitate the control of the excitation module (Fig. S6).

The aforementioned circuit configurations are implemented onto a Bluetooth-enabled flexible printed circuit board (FPCB), which in turn facilitates wireless and bilateral communication of user commands with a custom-developed interactive smartphone application (Fig. 4a-e). To power the FPCB, a single miniaturized rechargeable lithium-ion polymer battery with a nominal voltage of 3.7 V is used. To achieve a power-efficient system, the intended circuit configurations are implemented using the integrated circuit chips that are specifically designed for low-power applications. Based on preliminary characterization results, without further power optimization,

the envisioned simultaneous operations (*e.g.*, ACET actuation and bilateral wireless communication) demand supply current levels of approximately 50-100 mA. The battery's capacity should be selected in relation to the duration/frequency of intended operation as well as the desired ACET actuation performance. To illustrate the latter point, we characterized the delivered power for achieving different ACET mixing efficiencies (Table S1).

To realize on-body implementation of the ACET excitation, the electrical connections between the microfluidic and the FPCB modules can be established with a flat flexible cable and a vertically conductive tape or stretchable wires (Fig. 4c). To visualize the achievement of the ACET actuation, the aforementioned mixing characterization setup was adopted, where the reverse-bifurcated microfluidic configuration was placed on body (using two externally pumped model solutions: 1X transparent and 0.2X red-dyed PBS, Fig. S7a). As shown in Fig. S7b and Supplementary video 3 (with an array of three mixers), activation of the ACET excitation circuit leads to the mixing of the two neighboring laminar flow streams and rendering a homogenized fluid stream. Furthermore, the utility of the devised wearable ACET actuation interface for epidermally-retrieved biofluid actuation is shown by demonstrating *in-situ* mixing of the secreting sweat with an externally pumped model solution (0.2X red-dyed PBS). For localized sweat induction, the standard iontophoresis protocol was followed [32]. As illustrated in Fig. 4f, a sweat collection chamber is incorporated to harvest and route the secreting sweat through one inlet, while the model solution was pumped into the other inlet (where its flow rate was adjusted to match the sweat secretion rate, here, 1.5 μL/min). As shown in Fig. 4g, the results indicate that upon activation of the ACET actuation (3.5 V_{rms}), homogeneous mixing of the secreting sweat and the model solution streams was achieved, demonstrating the suitability of ACET actuation for biofluid manipulation.

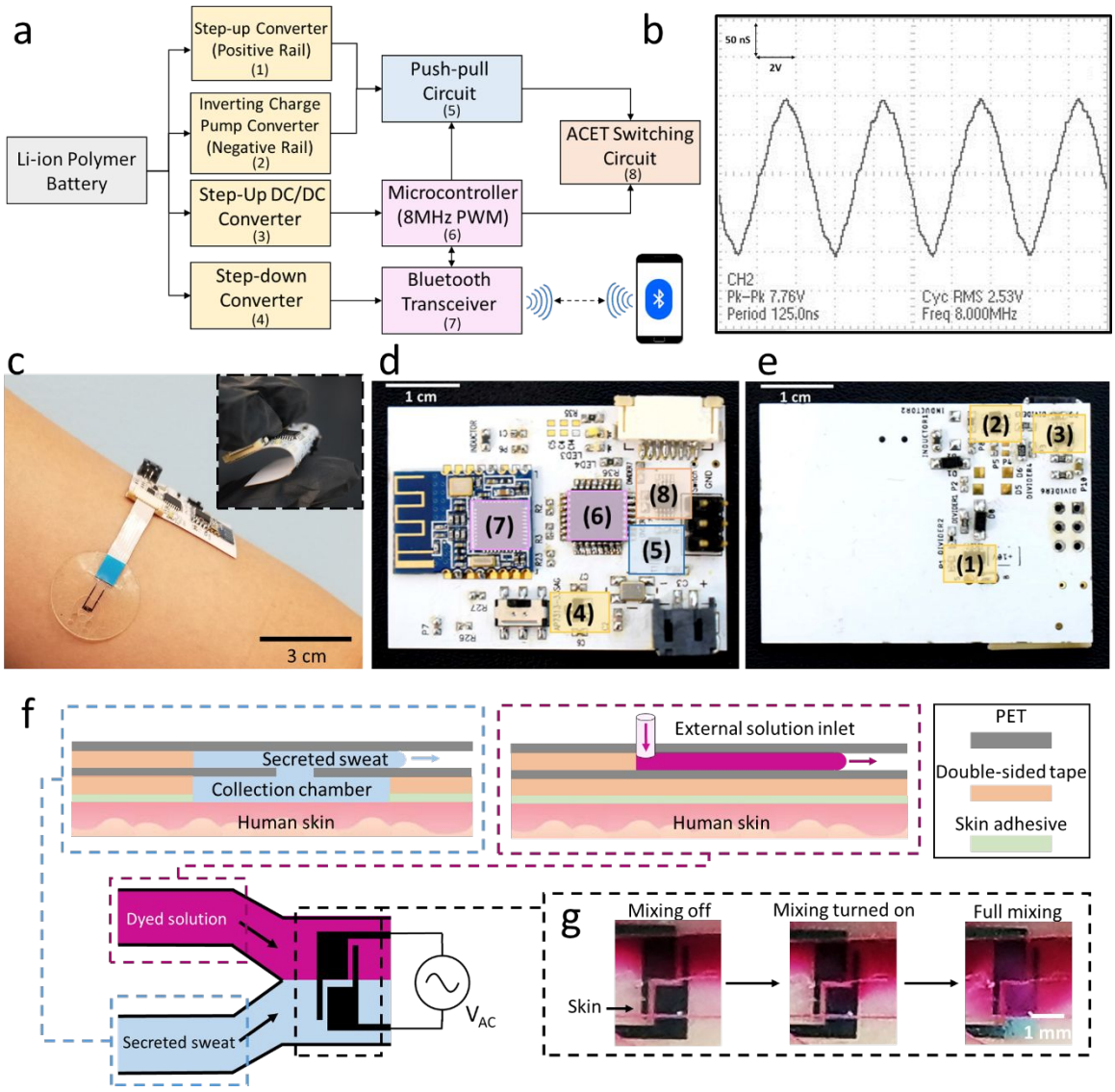

Figure 4. Wearable ACET excitation and visualization on-body. a) System level diagram of the ACET excitation circuit (numbers 1 through 7 indicate corresponding circuitries on the ensuing FPCB images). **b)** A representative push-pull circuit voltage output for ACET actuation. **c)** A representative assembled FPCB, integrated with the microfluidic device, placed on a human subject's forearm. **d)** Front view of the assembled FPCB. **e)** Rear-view of the assembled FPCB. **f)** Top view schematic of the experimental setup for the ACET mixing of secreting sweat with an externally pumped red-dyed solution. Corresponding side-views of the two inlets of the device-epidermal interface are shown atop. **g)** Sequential optical images of the on-body mixing of iontophoretically induced sweat with a red-dyed solution.

Conclusion

We report a wearable electrofluidic actuation platform which exploits the ACET effects to engineer biofluid flow profiles on-body. The wearable ACET flow is induced using corrosion-resistant electrode configurations (fabricated on a flexible substrate and embedded within a microfluidic module) and a custom-developed, wirelessly programmable high frequency (MHz) excitation circuitry. Various tunable flow profiles were demonstrated with the aid of the devised flexible ACET electrode configurations, where the induced profiles were in agreement with the ACET theory and simulation. The presented platform overcomes the limitations of previously demonstrated wearable bioanalytical devices in terms of lack of active control on biofluids, and enables the implementation of previously demonstrated lab-on-a-chip-based sample preparation and manipulation operations on-body. In this way, the devised platform creates new possibilities for the realization of complex assays in a wearable format, thus expanding the diversity and quantity of detectable target biomarkers.

Institutional Review Board (IRB) approval

The conducted human subject experiments were performed in compliance with the protocols that have been approved by the IRB at the University of California, Los Angeles (IRB#17-000170). All subjects gave written informed consent before participation in the study.

Author contributions

H.L. and S.E. conceived the idea and designed the experiments; H.L. led the experiments (with assistance from S.L., H.H., K.K., M.M, Y.W., Z.W., J.T., and S.E.); H.H. led the FPCB development efforts; S.L. led the COMSOL simulation; H.L., H.H., S.L., M.M., Y.W., and K.K. contributed to the development of analytical tools; H.L., H.H., S.L., C.Y., Y.Z., B.W., M.M., Y.W., K.K., W.Y. J.T., Z.W., X.C., and S.E. contributed to data analysis and interpretation; H.L., H.H., S.L., C.Y., and S.E. drafted the manuscript and all the authors provided feedback. S.E. supervised the study.

Conflicts of interest

There are no conflicts to declare.

Acknowledgements

This work was supported by the S.E.'s startup package provided by the UCLA Henry Samueli School of Engineering and Applied Sciences. Components of research are supported by the National Science Foundation (Award #1847729), Henry M. Jackson Foundation, Brain and Behavior Foundation (NARSAD Young Investigator Grant), and PhRMA Foundation (Research Starter Grant in Translational Medicine and Therapeutics). The authors appreciate the members of UCLA nanoelectronics research facility and Lux Lab (Doug Daniels) from UCLA Library for their help in device fabrication. We thank Amir Mohammad Hojaiji for assisting with designing the 3D concept figures.

References

1. W. Gao, S. Emaminejad, H. Y. Y. Nyein, S. Challa, K. Chen, A. Peck, H. M. Fahad, H. Ota, H. Shiraki, D. Kiriya, D.-H. Lien, G. A. Brooks, R. W. Davis and A. Javey, *Nature*, 2016, **529**, 509–514.
2. J. Heikenfeld, A. Jajack, J. Rogers, P. Gutruf, L. Tian, T. Pan, R. Li, M. Khine, J. Kim, J. Wang and J. Kim, *Lab Chip*, 2018, **18**, 217–248.
3. H. Lee, C. Song, Y. S. Hong, M. S. Kim, H. R. Cho, T. Kang, K. Shin, S. H. Choi, T. Hyeon and D.-H. Kim, *Science Advances*, 2017, 3, e1601314.
4. Y. Yang and W. Gao, *Chem. Soc. Rev.*, 2019, **48**, 1465–1491.
5. S. Emaminejad, W. Gao, E. Wu, Z. A. Davies, H. Yin Yin Nyein, S. Challa, S. P. Ryan, H. M. Fahad, K. Chen, Z. Shahpar, S. Talebi, C. Milla, A. Javey and R. W. Davis, *Proc. Natl. Acad. Sci. U. S. A.*, 2017, **114**, 4625–4630.
6. J. Heikenfeld, A. Jajack, B. Feldman, S. W. Granger, S. Gaitonde, G. Begtrup and B. A. Katchman, *Nat. Biotechnol.*, 2019, **37**, 407–419.
7. J. Kim, A. S. Campbell, B. E.-F. de Ávila and J. Wang, *Nat. Biotechnol.*, 2019, **37**, 389–406.
8. A. Martín, J. Kim, J. F. Kurniawan, J. R. Sempionatto, J. R. Moreto, G. Tang, A. S. Campbell, A. Shin, M. Y. Lee, X. Liu and J. Wang, *ACS Sens*, 2017, **2**, 1860–1868.
9. J. R. Sempionatto, A. Martin, L. García-Carmona, A. Barfidokht, J. F. Kurniawan, J. R. Moreto, G. Tang, A. Shin, X. Liu, A. Escarpa and J. Wang, *Electroanalysis*, 2019, 31, 239–245.
10. H. Y. Y. Nyein, L.-C. Tai, Q. P. Ngo, M. Chao, G. B. Zhang, W. Gao, M. Bariya, J. Bullock, H. Kim, H. M. Fahad and A. Javey, *ACS Sens*, 2018, **3**, 944–952.

11. A. Koh, D. Kang, Y. Xue, S. Lee, R. M. Pielak, J. Kim, T. Hwang, S. Min, A. Banks, P. Bastien, M. C. Manco, L. Wang, K. R. Ammann, K.-I. Jang, P. Won, S. Han, R. Ghaffari, U. Paik, M. J. Slepian, G. Balooch, Y. Huang and J. A. Rogers, *Sci. Transl. Med.*, 2016, **8**, 366ra165.
12. Y. Zhang, H. Guo, S. B. Kim, Y. Wu, D. Ostojich, S. H. Park, X. Wang, Z. Weng, R. Li, A. J. Bandodkar, Y. Sekine, J. Choi, S. Xu, S. Quaggin, R. Ghaffari and J. A. Rogers, *Lab Chip*, 2019, **19**, 1545–1555.
13. Y. Sekine, S. B. Kim, Y. Zhang, A. J. Bandodkar, S. Xu, J. Choi, M. Irie, T. R. Ray, P. Kohli, N. Kozai, T. Sugita, Y. Wu, K. Lee, K.-T. Lee, R. Ghaffari and J. A. Rogers, *Lab Chip*, 2018, **18**, 2178–2186.
14. J. Choi, A. J. Bandodkar, J. T. Reeder, T. R. Ray, A. Turnquist, S. B. Kim, N. Nyberg, A. Hourlier-Fargette, J. B. Model, A. J. Aranyosi, S. Xu, R. Ghaffari and J. A. Rogers, *ACS Sens*, 2019, **4**, 379–388.
15. A. D. Stroock, S. K. W. Dertinger, A. Ajdari, I. Mezic, H. A. Stone and G. M. Whitesides, *Science*, 2002, **295**, 647–651.
16. L.-H. Lu, K. S. Ryu and C. Liu, *Journal of Microelectromechanical Systems*, 2002, 11, 462–469.
17. G. S. Jeong, S. Chung, C.-B. Kim and S.-H. Lee, *The Analyst,* 2010, 135, 460.
18. T. Frommelt, M. Kostur, M. Wenzel-Schäfer, P. Talkner, P. Hänggi and A. Wixforth, *Phys. Rev. Lett.*, 2008, **100**, 034502.
19. P. K. Wong, T. -H. Wang, J. H. Deval and C. -M. Ho, *IEEE/ASME Transactions on Mechatronics*, 2004, 9, 366–376.
20. J. Wu, M. Lian and K. Yang, *Applied Physics Letters*, 2007, 90, 234103.

21. E. Du and S. Manoochehri, *Journal of Applied Physics*, 2008, 104, 064902.

22. S. Loire, P. Kauffmann, I. Mezić and C. D. Meinhart, *Journal of Physics D: Applied Physics*, 2012, 45, 185301.

23. M. L. Y. Sin, V. Gau, J. C. Liao and P. K. Wong, *JALA Charlottesv. Va*, 2010, **15**, 426–432.

24. C.-C. Chang and R.-J. Yang, *Microfluidics and Nanofluidics*, 2007, 3, 501–525.

25. H.-Y. Wu and C.-H. Liu, *Sensors and Actuators A: Physical*, 2005, 118, 107–115.

26. S.-H. Huang, S.-K. Wang, H. S. Khoo and F.-G. Tseng, *TRANSDUCERS 2007 - 2007 International Solid-State Sensors, Actuators and Microsystems Conference*, 2007.

27. Y. Lu, T. Liu, A. C. Lamanda, M. L. Y. Sin, V. Gau, J. C. Liao and P. K. Wong, *J. Lab. Autom.*, 2015, **20**, 611–620.

28. S. Dekker, P. K. Isgor, T. Feijten, L. I. Segerink and M. Odijk, *Microsyst Nanoeng*, 2018, **4**, 34.

29. C. Peng, Z. Zhang, C.-J. C. J. Kim and Y. S. Ju, *Lab Chip*, 2014, **14**, 1117–1122.

30. S. K. Cho, H. Moon and C.-J. Kim, *Journal of Microelectromechanical Systems*, 2003, 12, 70–80.

31. A. Castellanos, A. Ramos, A. González, N. G. Green and H. Morgan, Journal of Physics D: Applied Physics, 2003, 36, 2584–2597.

32. [anonymus Ac06619969], Sweat Testing: Sample Collection and Quantitative Analysis, Approved Guideline, 2000.

33. A. González, A. Ramos, H. Morgan, N. G. Green and A. Castellanos, Journal of Fluid Mechanics, 2006, 564, 415.

34. C. D. Hodgman and S. C. Lind, The Journal of Physical and Colloid Chemistry, 1949, 53, 1139–1139.